PERGAMON

Computers & Fluids 30 (2001) 711–735

computers & fluids

www.elsevier.com/locate/compfluid

Analysis of micro-scale gas flows with pressure boundaries using direct simulation Monte Carlo method

J.-S. Wu *, K.-C. Tseng

Department of Mechanical Engineering, National Chiao-Tung University, 1001 Ta-Hsueh Road, Hsinchu 30050, Taiwan

Received 3 January 2000; received in revised form 15 May 2000; accepted 14 August 2000

Abstract

The development of a two-dimensional direct simulation Monte Carlo program for pressure boundaries using unstructured cells and its applications to typical micro-scale gas flows are described. For the molecular collision kinetics, variable hard sphere molecular model and no time counter collision sampling scheme are used, while the cell-by-cell particle tracing technique is implemented for particle movement. The program has been verified by comparison of simulated equilibrium collision frequency with theoretical value and by comparison of simulated non-equilibrium profiles of one-dimensional normal shock with previous reported work. Applications to micro-scale gas flows includes micro-manifold, micro-nozzle and slider air bearing. The aim is to further test the treatment of pressure boundaries, developed previously by the first author, by particle flux conservation for gas flows involving many exits, complicated geometries and moving boundaries. For micro-manifold gas flows, excellent mass flow conservation between the inlet and two exits is obtained at low subsonic flows. For micro-nozzle gas flows, with fixed inlet pressure, the mass flow rate increases with decreasing pressure ratio (exit to inlet), but remains essentially the same at pressure ratios much lower than that obtained by continuum inviscid analysis. For higher specified pressure ratios, the locations of maximum Mach number moves further downstream as the pressure ratio decreases; while, for lower specified pressure ratios, the Mach number increases all the way through the nozzle to the exit. Eventually, supersonic speed is observed at the exit for pressure ratios equal to or less than 0.143. Finally, for slider air bearing gas flows of the computer hard drive, the simulated gas pressures, at different rotating speeds, agree very well with previous studies. However, there exists strong translational non-equilibrium in the gas flows at the high rotating speeds. The applicability of the treatment of pressure boundaries using the equilibrium Maxwell–Boltzmann distribution function is discussed in terms of the magnitude of the local Knudsen number at the pressure boundary for micro-nozzles and slider air bearing applications.

* Corresponding author. Tel.: +886-3-5731693; fax: +886-3-5720634.
E-mail address: chongsin@cc.nctu.edu.tw (J.-S. Wu).

0045-7930/01/$ - see front matter
PII: S0045-7930(00)00029-3

Keywords: Direct simulation Monte Carlo; Knudsen number; Micro-nozzle; Micro-manifold; Slider air bearing; Pressure boundary

1. Introduction

Micro-electro-mechanical systems (MEMS) are becoming prevalent both in commercial and industrial research due to the rapid growth and developments in the semiconductor industry. MEMS are the field with strong multi-disciplinary research needs. Applications for these devices include consumer products (e.g., airbag triggers, micro-mirror displays), industrial and medical tools (e.g., micro-valves, micro-motors), and instrumentation (e.g., micro-pressure sensors, micro-shear stress sensors) [1].

The shrinking size of MEMS (order of a micron) has several advantages over the corresponding macro-scale systems. First, they can be fabricated quite inexpensive and in large quantities, borrowing mature techniques developed in the semiconductor industry. Second, the miniature inertia (due to small size) allows them to respond very quickly to excitation, enabling the fabrication of actuators and sensors with frequency responses previously unimaginable for related mechanical systems [2].

In the past, most research was conducted concerning the electrical and mechanical properties of MEMS. Relatively few researches [15,20–22,28] focused on the thermal and fluid effects on MEMS performance, including rarefaction, thermal creep and compressibility. Hence, the understanding of these physical effects is very important for the design optimization of these very small-scale devices.

Most research on the analysis of thermal and fluid problems in MEMS devices has relied on computational or theoretical approaches due to the experimental difficulties presented in a micro-dimensional environment. The computational and analytical tools available are generally based on the Navier–Stokes equations. A crucial underlying assumption of these equations is that the fluid may be treated as a continuum rather than as a collection of discrete particles, as is the case with the more difficult to solve Boltzmann equation [3]. Based on the continuum assumptions, flows can be described in terms of macroscopic variables such as temperature and pressure rather than microscopic variables such as molecular velocity distribution functions.

Unfortunately, continuum assumption begins to break down when the mean free path (λ, average distance traveled by molecules before collision) becomes comparable to flow characteristic length (L). The ratio of these two quantities is known as Knudsen number ($Kn = \lambda/L$) and is usually used to indicate the degree of rarefaction. Traditionally, flows are divided into four regimes as follows [4]: $Kn < 0.01$ (continuum), $0.01 < Kn < 0.1$ (slip flow), $0.1 < Kn < 3$ (transitional flow) and $Kn > 3$ (free-molecular flow). As Kn increases, the rarefaction becomes important and even dominates the flow behavior. Hence, the N–S based computational fluid dynamics (CFD) techniques are often inappropriate for higher Kn flows, such as slip flow, transitional flow and free-molecular flow.

For most MEMS flows, the Knudsen numbers are generally located in the slip-flow and transitional-flow regimes due to their micro-scales, even at atmospheric condition. An example of such a micro-scale device is a side-driven micro-motor [5,6]. The typical gap between the base and the rotor is 3 μm, the corresponding *Kn* equal to 0.05. Another example of large *Kn* is the modern Winchester-type hard disk drive mechanism, where the read/write head floats about 60 nm or less above the surface of the spinning platter [7]. The corresponding *Kn* is equal to 1.1. Hence, the rarefaction effects, often neglected in traditional analysis, have to be carefully considered and modeled in micro-scale gas flows.

The direct simulation Monte Carlo (DSMC) method, first introduced by Bird [8,9], has been recognized as a defacto method for studying rarefied gas dynamics. It has been applied very successfully to rarefied hypersonic flows [8,9] and other more fundamental scientific problems, such as flow instabilities [10,11]. In addition to the space science applications, it has also been utilized in the analysis of ultra-high vacuum technology [12–14]. Very recently, it was applied to rarefied internal gas flow problems such as channel, pipe and duct flows and the results agree very well with experiments [15]. Most importantly, DSMC is the only practical way to deal with flows in the transitional regime, without resorting to the difficult Boltzmann equation, which requires modeling an integral–differential (collision) term. Hence, for the analysis of rarefied gas dynamics, the DSMC method has proved to be a very powerful tool.

Most applications of the DSMC have used *structured grids* [8,9] to discretize the physical domain. For problems with complicated geometry, multi-block meshing techniques were developed first by Bird [9], which involved two steps: dividing the flow field into several blocks followed by discretizing each block into quadrilateral (two-dimensional) or cubic (three-dimensional) meshes. Subsequent research has been directed to develop alternative meshing techniques such as the coordinate transformation method by Merkle [24], the body-fitted coordinate system by Shimada and Abe [25] and the transfinite interpolation method by Olynick et al. [26]. However, all of these still used structured grids. It is much easier to program the code using structured grids, however, it requires tremendous problem specific modification. To alleviate such restriction, an *unstructured grid* system is an alternative choice, although it might be computationally more expensive. Boyd's group [16–18] has applied such techniques to compute thruster plumes produced by spacecraft and found that the results are very satisfactory. Wilmoth et al. [19] have used two types of grid (unstructured tetrahedral and structured Cartesian grids) to compute the low-density, hypersonic flows about reusable launch vehicle. Both methods were shown to give comparable results; however, it was concluded that unstructured grid offers certain advantages for grid refinement and structured grid appears to offer greater overall advantages.

Wong and Harvey [27] have further employed remeshing adaptive grid techniques in combination with unstructured meshes to study flows with highly non-uniform density. However, the above-mentioned studies were mostly applied to high-speed gas flows.

For low-speed gas flow applications, Piekos and Breuer [20] used DSMC to analyze the gas dynamics of micro-mechanical devices using unstructured grids. In their research, they developed a special way to accommodate the inflow/outflow pressure boundary conditions. However, Ref. [20]'s boundary condition treatment is not as effective as they claimed when treating pressure boundaries; furthermore, it has not been tested in more complicated applications. Nance et al. [22] adopted the theory of characteristics from continuum gas dynamics and incorporated the

procedure in the DSMC method to handle the pressure specified micro-channel gas flows at a subsonic exit.

Alexander et al. [28] used DSMC to simulate the nano-scale gas flow of a computer hard drive slider air bearing. The results showed that the gas pressure inside the air bearing is not uniform. The pressure generally increases from atmospheric level with distance in the disk rotating direction, obtains its maximum value near the end of the write/read head and decreases rapidly to the atmospheric value. The location of the maximum pressure value moves further downstream with increasing disk speed. In treating these pressure boundary conditions, they have also designed a special way to update the inlet and exit speeds such that the inlet and exit pressures are the same as specified. However, it is not clear how they precisely implemented the treatment.

Recently, Wu et al. [23] developed an effective way to process pressure boundaries with the DSMC method and successfully applied it to gas flows with simple geometries such as micro-channel and backward-facing micro-step configuration. The developed pressure boundary treatment is inherently mass conserved because particle flux conservation is applied at each pressure boundary, assuming thermal equilibrium. Also it has been demonstrated [23] that the procedure requires fewer time steps to "converge" to the steady-state solution as compared with the approach of Nance et al. [22]. However, their application to gas flows with more complicated geometry or with many inlets and exits are yet to be verified. In addition, it is also crucial to understand its limit of applicability in rarefied or micro-scale gas flows.

From the previous review, we see a need to develop an efficient and accurate simulation/analysis tool for thermal/fluid problems in micro-scale gas flows with pressure boundaries. Thus, the objectives of the current research are to develop a DSMC code using an unstructured grid system and to apply the code to several micro-scale gas flows, including micro-manifold, micro-nozzle and computer hard drive slider air bearing by using the pressure boundary treatment developed previously [23].

2. Numerical method

2.1. The direct simulation Monte Carlo method

Due to the expected rarefaction caused by the very small size of micro-scale or nano-scale devices, the current research is performed using the DSMC [8,9] method, which is a particle-based method. The basic idea of DSMC is to calculate practical gas flows through the use of a method that has a physical rather than a mathematical foundation. The assumptions of molecular chaos and a dilute gas are required by both the Boltzmann formulation and the DSMC method [8]. The molecules move in the simulated physical domain so that the physical time is a parameter in the simulation and all flows are computed as unsteady flows. An important feature of DSMC is that the molecular motion and the intermolecular collisions are uncoupled over the time intervals that are much smaller than the mean collision time. Both the collision between molecules and the interaction between molecules and solid boundaries are computed on a probabilistic basis and, hence, this method makes extensive use of random numbers. In most practical applications, the number of simulated molecules is extremely small compared with the number of real molecules.

The details of the procedures, the consequences of the computational approximations can be found in Bird [8,9]. In the current study, the variable hard sphere (VHS) molecular model [8] and the no time counter (NTC) [8] collision sampling technique are used to simulate the molecular collision kinetics except for the computer hard disk slider air bearing problem. Note that the corresponding molecular data including reference diameter (d_{ref}), reference temperature (T_{ref}), and the viscosity temperature exponent (ω) for each species are taken from those listed in Ref. [8]. Solid walls for all cases considered in this study are assumed to be fully diffusive (100% thermal accommodation) and are equal to 300 K unless otherwise specified.

2.2. Pressure boundary condition treatment

In order to perform accurate simulation for inflow/outflow pressure boundaries, general procedure for treating these conditions by using the concept of particle flux conservation has been developed and incorporated into the basic DSMC algorithm [23]. The basic idea is to update the inflow and outflow velocities by applying particle flux conservation, assuming thermal equilibrium, at each pressure boundary, such that the mass flow rate conserves automatically and the simulated boundary pressures coincide with the imposed values. Note that the assumption of thermal equilibrium at the pressure boundaries may not be justified for very high local Knudsen number flow, which can be seen clearly from the results presented later for specific test cases. However, we will show that the thermal equilibrium is correct for most MEMS related subsonic flows. For completeness, the implementation of updating the pressure boundary conditions is briefly described. For more details, see Ref. [23].

For a given mean speed (V) and temperature (T), the particle flux across a boundary surface with area A in a particular direction θ with the surface normal can be determined, assuming equilibrium Maxwell–Boltzmann distribution [8,9], as

$$\frac{\dot{N}}{A} = \frac{nV_{\mathrm{mp}}\{\exp(-q^2) + \sqrt{\pi}q[1 + \mathrm{erf}(q)]\}}{2\sqrt{\pi}}, \tag{1a}$$

where

$$q = \frac{V}{V_{\mathrm{mp}}}\cos\theta, \tag{1b}$$

$$V_{\mathrm{mp}} = \sqrt{\frac{2kT}{m}}, \tag{1c}$$

m is the molecular mass, n is the number density, V_{mp} is the most probable speed and k is the Boltzmann constant.

At the inflow pressure boundary, inflow pressure p_{i} and temperature T_{i} are both known and thus the inflow number density n_{i} is known. By applying the particle flux conservation for each cell interface $\boldsymbol{m}$ (area A_m) at the inflow pressure boundary, the updated inflow streamwise velocity at cell $\boldsymbol{m}$ (outside the flow domain) is computed as

$$(u_{\mathrm{i}})_m = \frac{\dot{N}_+ - \dot{N}_-}{n_{\mathrm{i}}A_m}, \tag{2}$$

where $\dot{N}_+$ and $\dot{N}_-$ are the computed particle flux (Eqs. (1a)–(1c)) into and out of the flow domain (cell ***m***) at the inflow pressure boundary using the updated $(u_i)_m$ and sampled streamwise velocity at each inflow boundary cell ***m***, respectively, with number density n_i and temperature T_i. The value of $(u_i)_m$ and the sampled streamwise velocity for each inflow cell ***m*** will be varied during the simulation and eventually attain approximately the same value as steady state is reached.

At the outflow pressure boundary, all fluid properties except pressure are computed from the simulation. Again, we apply the concept of particle flux conservation rather than the theory of characteristics [22] for each cell at the outflow pressure boundary. Then, a similar procedure treating inflow conditions is carried out for updating outflow streamwise velocity $(u_e)_m$ (outside the flow domain) for each outflow boundary cell ***m***. Note that the outflow temperature for each cell interface is not given in advance and is set to the temperature sampled inside for each outflow boundary cell ***m*** during simulation. Additionally, the outflow number density is computed using the equation of state.

By applying the above procedures at the inflow and outflow pressure boundaries, the simulated inflow and outflow pressures are found to be consistent with the specified inflow and outflow pressures and mass conservation holds automatically. In Ref. [23], the results of a micro-channel flow using the current approach agreed very well with those of Nance et al. [22] and it was shown that fewer samplings are required to "converge" to the steady-state solution. Typical pressure profile, in a micro-channel, as a function of streamwise location from the current pressure boundary treatment along with that from Ref. [22] is shown in Fig. 1 with the following flow conditions: argon gas (VHS gas), inlet temperature $T_i = 300$ K, pressure ratio $P_i/P_e = 3$ ($P_i = 160.839$ kPa) and aspect ratio $L/H = 5$ ($L = 5$ μm). From the excellent agreement between these results, we are confident that the results of the current approach applying particle flux conservation can at least be consistent with that of Nance et al. [22] using the method of characteristics concept.

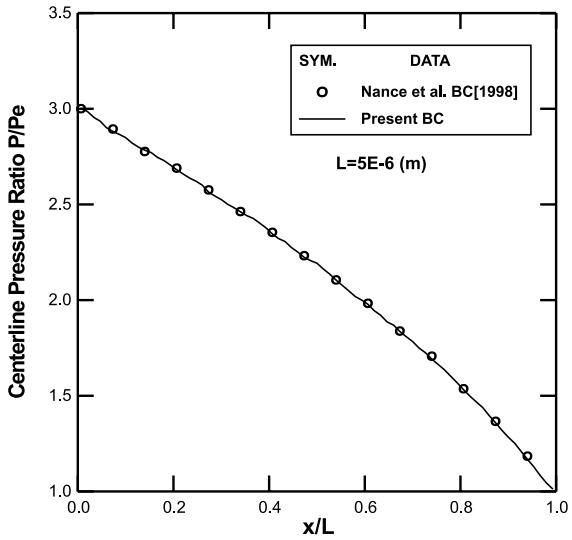

Fig. 1. Comparison of the simulated pressure profiles for the pressure boundary treatment by Nance et al. [22] and the current approach.

2.3. Other concerns

The macroscopic quantities such as mean velocities and temperature are sampled and averaged from cells, which may be triangular, quadrilateral or hybrid with both. Because of the unstructured meshes used, cell-by-cell particle tracing technique similar to Piekos and Breuer [20,21] is adopted to locate the final particle position at the end of each time step during computation. This might increase the computational load in locating the cell number of the final particle position during each time step, however, it offers the greatest flexibility of handling different types of boundary conditions and required much less problem specific change in programming. In practice, the computational time required using a particle tracing technique is comparable to those of structured mesh with careful selection of time step and cell sizes using the same number of simulated particles.

3. Results and discussion

3.1. Code verification

For code verification, we have computed the equilibrium collision frequency within an adiabatic enclosure, non-equilibrium profiles within a one-dimensional (1-D) normal shock, and sensitivity test by using different mesh types. Results from these investigations are briefly described.

First, we computed the equilibrium collision frequency of argon and helium, respectively, in a square enclosure with adiabatic wall conditions. The time step used is about 1/6 of the mean collision time and the cell size is about 1/2 of the mean free path. This rule of thumb of selecting simulation time step applies to all cases studied in this research. Further refinement of cell size does not improve the results much. The flow was run for 1000 time steps to allow any initial condition effects to die out, then sampled every two time steps until 2000 samples were obtained. The results, insensitive for argon and helium, show that the computed values are within 1%, 1.9%, 3% and 5% of theoretical values, when the average number of particle per cell equals 100, 50, 20 and 10, respectively. These findings are comparable to those of Piekos [21].

Second, a 1-D Mach 8 argon normal shock is simulated using the stabilization technique proposed by Bird [8]. The upstream velocity, temperature and number density are equal to 2548.6 m/s, 293 K and 1E20 particles/m^3, respectively. Typical results are illustrated in Fig. 2 along with those obtained by Bird [8]. Computed temperature profiles illustrate that there exists strongly non-equilibrium between the normal and parallel translational degrees of freedom at such high Mach number. The present results are in good agreement with Bird [8].

Finally, the code is used to predict the argon gas flows in micro-channels using triangular, quadrilateral and hybrid (triangular and quadrilateral) meshes. The purpose is to test the sensitivity of the results to the type of meshes used and the particle tracing technique for handling the different types of meshes. Results of centerline streamwise velocities are presented in Fig. 3, where non-dimensional location is defined as x/L with the length of the channel $L = 22.5$ μm and the channel height is 4.5 μm. The inlet pressure and temperature are set as 7.146 kPa and 300 K, respectively, with inlet-to-exit pressure ratio equal to 3. For the three meshes tested, the simulated

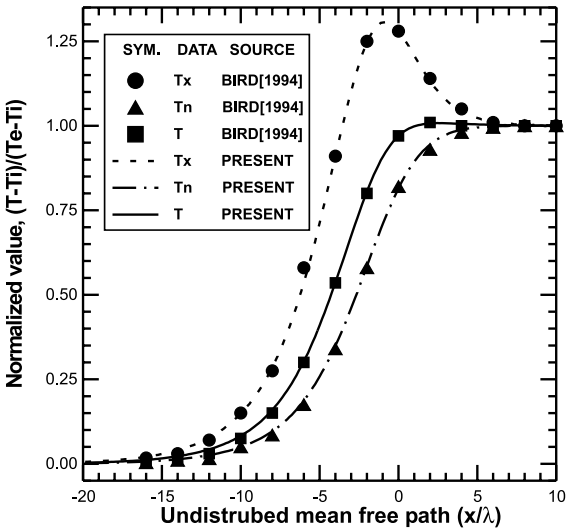

Fig. 2. Computed temperatures in a $Ma = 8$ argon shock, including parallel and normal components.

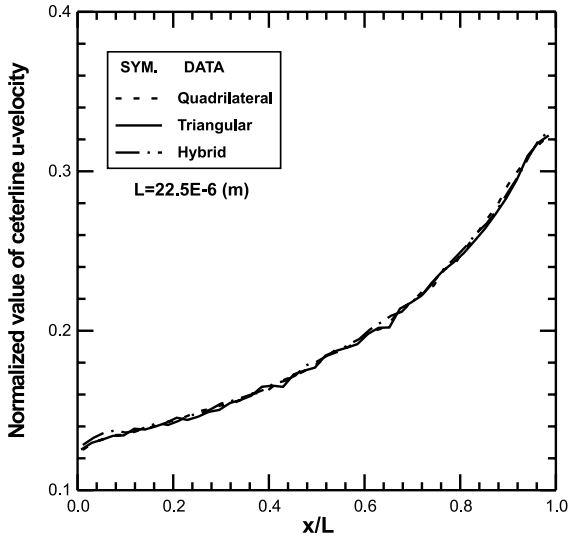

Fig. 3. Micro-channel centerline u-velocity profiles calculated with different meshes ($L = 22.5$ μm).

centerline streamwise velocities coincide very well with each other. This agreement applies to other fluid properties as well. This demonstrates that the current code is mesh-type insensitive. Thus, the current DSMC code is verified to be accurate in tracing particles in unstructured meshes and in predicting both the equilibrium and non-equilibrium phenomena in rarefied gas dynamics. For clarity of discussion in the following, all subscripts with "i" and "e" stand for inlet and exit of the flows, respectively.

3.2. T-shape micro-manifold

A micro-manifold is chosen as the first application case for the purpose of testing the general treatment of pressure boundaries with multiple exits, a device with potential applications in medical technology. The sketch of a T-shaped micro-manifold is shown in Fig. 4 with one inlet and two exits, where exit 1 is at the upper right hand side (horizontal channel) and exit 2 at the lower bottom side (vertical channel). For the current simulation, $L/h_i = 7$, $H/h_i = 3$, $h_i = h_{e1} = h_{e2}$, and $h_i = 1$ μm. The inlet pressure is fixed and the pressures at exits 1 and 2 are varied such that the pressure ratios between the inlet and exits are 3:1:1 (case I), 3:1:2 (case II) and 3:2:1 (case III), respectively. Argon is the working gas with the inlet value (uniform) of temperature and pressure equal to 300 K and 26.79 kPa, respectively. The resulting Knudsen number based on the inlet conditions is 0.2. The initial conditions inside the micro-manifold are set as follows: zero mean velocities, uniform temperatures as T_i and uniform number densities as n_i. The simulation time step used is 8.33×10^{-11} s.

Table 1 shows the specified, simulated pressures and their difference at the inlet and exits for all the three cases considered. Note that the simulated pressures are computed from the average of inlet or exit boundary cells with almost negligible gradients across the channel. From the results, the simulated pressures are generally within 1.2% of those specified at the inlet and exits. This implies that the treatment of pressure boundaries by applying flux conservation is successful in handling the micro-manifold with single inlet and multiple exits at low subsonic flows.

Typical normalized mass flow rates as a function of time are presented in Fig. 5 for the case of specified pressures, $P_i{:}P_{e1}{:}P_{e2} = 3{:}1{:}1$ (case I). This illustration monitors how the mass flow rate at each pressure boundary converges to its steady value and how the total mass flow conserves as well. Before the sampling starts, the mass flow rates at the inlet and exits fluctuates violently (sometimes negative, not shown in the figure); however, after the sampling starts, the corresponding mass low rates begins to converge to the steady values. The sum of the exit flow rates is greater than the inlet flow rate before reaching steady state (for time less than approximately 0.01 s in Fig. 5) because of the initial conditions imposed. The initial sum of the exit mass flow rates is larger than the inlet mass flow rate because of the larger difference between the initial flow field density (the same as n_i) and the initial boundary density at the exits. We have tried different initial

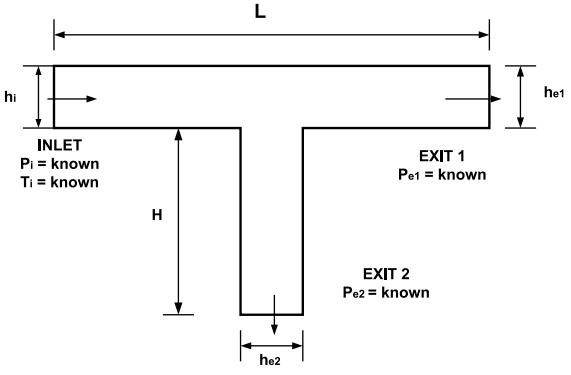

Fig. 4. Sketch of T-shape micro-manifold ($h_i = h_{e1} = h_{e2} = 1$ μm, $L/H = 7/3$, $L/h_i = 7$, $K_{n_i} = 0.2$).

Table 1
Comparison of simulated and specified I/O pressures for T-shape micro-manifolds

Case	P_i:P_{e1}:-P_{e2}	Inlet[a]			Exit 1[a]			Exit 2[a]		
		$P_{spc.}$[b]	$P_{sim.}$[c]	$(P_{sim.}-P_{spc.})/P_{spc.}$ (%)	$P_{spc.}$	$P_{sim.}$	$(P_{sim.}-P_{spc.})/P_{spc.}$ (%)	$P_{spc.}$	$P_{sim.}$	$(P_{sim.}-P_{spc.})/P_{spc.}$ (%)
I	3:1:1	1.0	1.001	0.10	0.333	0.335	0.60	0.333	0.336	0.90
II	3:1:2	1.0	1.001	0.10	0.333	0.337	1.20	0.667	0.668	0.15
III	3:2:1	1.0	1.004	0.40	0.667	0.668	0.15	0.333	0.336	0.90

[a] All pressure values are normalized to inlet specified pressure value, $P_i = 26.79$ kPa.
[b] Subscript "spc." represents the specified value.
[c] Subscript "sim." represents the simulated value.

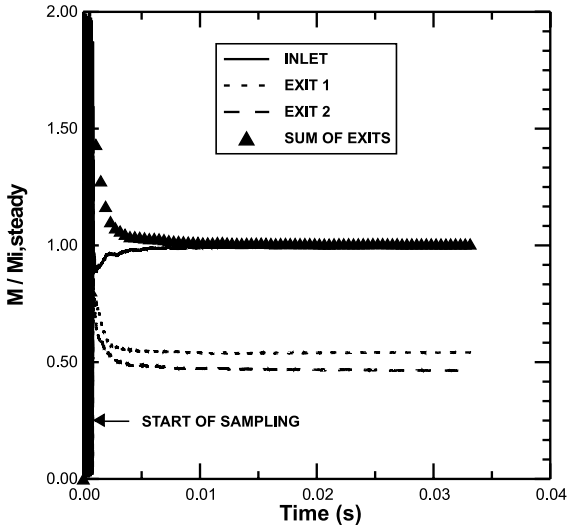

Fig. 5. The normalized mass flow rate for a T-shape micro-manifold with P_i:P_{e1}:P_{e2} = 3:1:1 and $P_i = 26.79$ kPa.

conditions by varying the initial uniform density in the flow field from vacuum (lowest) to inlet value (highest). As expected, the final steady-state mass flow rates are the same for all cases. By applying the particle flux conservation at each pressure boundary, the mass flow rate summation of exits 1 and 2 quickly approaches the mass flow rate of the inlet, within 0.6% in this case. Also about 54% of the mass flows out of exit 1 (horizontal channel). This behavior is mainly due to the larger pressure drop required for the gas particles to turn into the vertical exit 2. Consequently, the mass flow rate is less at exit 2, as illustrated in Fig. 5. Table 2 records the normalized steady mass flow rates into or out of each pressure boundary and the total mass flow rate for the three cases considered in the present study. As tabulated, the summation of simulated mass flow rates at exit 1 and exit 2 are within 0.9% of the inlet mass flow rates for the three cases tested. Mass flow rate decreases with increasing exit pressures for either exit 1 or 2 as expected. However, as specified pressure at exit 2 is higher than that at exit 1 (case II), most gas particles (more than 97%) flow directly into exit 1 (horizontal channel), which effectively blocks exit 2 (vertical channel).

General flow properties for the T-shaped micro-manifold, including velocity vector and u-velocity, v-velocity, Mach number, temperature and pressure contours, are illustrated in Fig. 6a–f

Table 2
Comparison of simulated mass flux of inlet and exits for T-shape micro-manifolds

Case	P_i:P_{e1}:P_{e2}	Inlet		Exit 1	Exit 2	Summation	Error
		$(\dot{m}_i/\dot{m}_{i,I})$	$(\dot{m}_i/\dot{m}_i)$	$(\dot{m}_{e1}/\dot{m}_i)$	$(\dot{m}_{e2}/\dot{m}_i)$	$(\dot{m}_{e1}+\dot{m}_{e2})/\dot{m}_i$	$(\dot{m}_{e1}+\dot{m}_{e2}-\dot{m}_i)/\dot{m}_i$ (%)
I	3:1:1	1.00	1.00	0.541	0.465	1.006	0.60
II	3:1:2	0.755	1.00	0.981	0.028	1.009	0.90
II	3:2:1	0.751	1.00	0.098	0.910	1.008	0.80

with P_i:P_{e1}:P_{e2} = 3:1:1. From Fig. 6a–c, we can see that gas flow accelerates gradually in the horizontal channel and achieves maximum speed at about 0.17 times the most probable speed based on inlet conditions, c_{mpi}, at the turning corner and then decelerates rapidly across the corner region and finally accelerates gradually again further downstream in the horizontal channel with a centerline exit speed at about $0.17c_{mpi}$. Similarly, the gas flow from the inlet of the horizontal channel accelerates across the corner region down to the exit 2 in the vertical channel with a smaller centerline exit speed (about $0.15c_{mpi}$) than that of exit 1. However, at this flow condition with the same pressures at both the exits, more gas particles flow into exit 1 than exit 2 (about 8% more, as discussed earlier) since a higher pressure drop for the gas flowing into exit 2 is required at the turning corner (larger pressure gradient), as can be seen from Fig. 6f. Therefore, the Mach number at the center part of exit 1 ($\sim$0.20) is higher than that ($\sim$0.17) at the center part of exit 2 (Fig. 6d). Also appreciable slip velocities at the solid wall, in the range of 0.06–$0.12c_{mpi}$, are observed at the inlet Knudsen number of 0.2. The simulated temperature field (Fig. 6e) is noisier than the velocity field, which is expected due to the low-speed flows involved and the large statistical variance of the instantaneous particle velocities used in obtaining the temperature data. The resulting temperature is almost uniform at the inlet temperature, except for the 3–5% drop near the exit centers caused by gas expansion. Finally, the pressure contours, as shown in Fig. 6f, illustrate the larger pressure gradient in the first half of the horizontal channel, while a much smaller value is observed in the second half of the horizontal channel and vertical channel. That is, most of the pressure drop occurs before the corner region in the horizontal channel and this also explains that the small subsonic speeds obtained at both exits 1 and 2.

Although there is no direct experimental data or theoretical prediction available to support the simulation conducted in the T-shaped micro-manifold, the physical trends qualitatively coincide with physical expectation. Thus, the generality of the pressure boundary treatment, using particle flux conservation, for multiple inlet and exits is at least qualitatively established.

3.3. Micro-nozzle

A micro-nozzle is selected as the second tested case because of its complex geometry and its potential for application as a MEMS device – micro-thrusters on spacecraft, for example. Additionally, this might serve as a test case to identify the limit of applicability of pressure boundary treatment [23], assuming thermal equilibrium, and results are presented later that clearly identify the problems at large Knudsen number flows. A micro-nozzle with area ratio (ratio of inlet to throat area; AR, hereafter) of 2 is considered. The dimensions are shown in Fig. 7. $L/h = 6.0$, where L and h are the nozzle length and throat height, respectively, and $h = 1$ μm. The inlet pressure, P_i, remains fixed at 80.4 kPa, while the specified exit pressure, P_e, is reduced such that

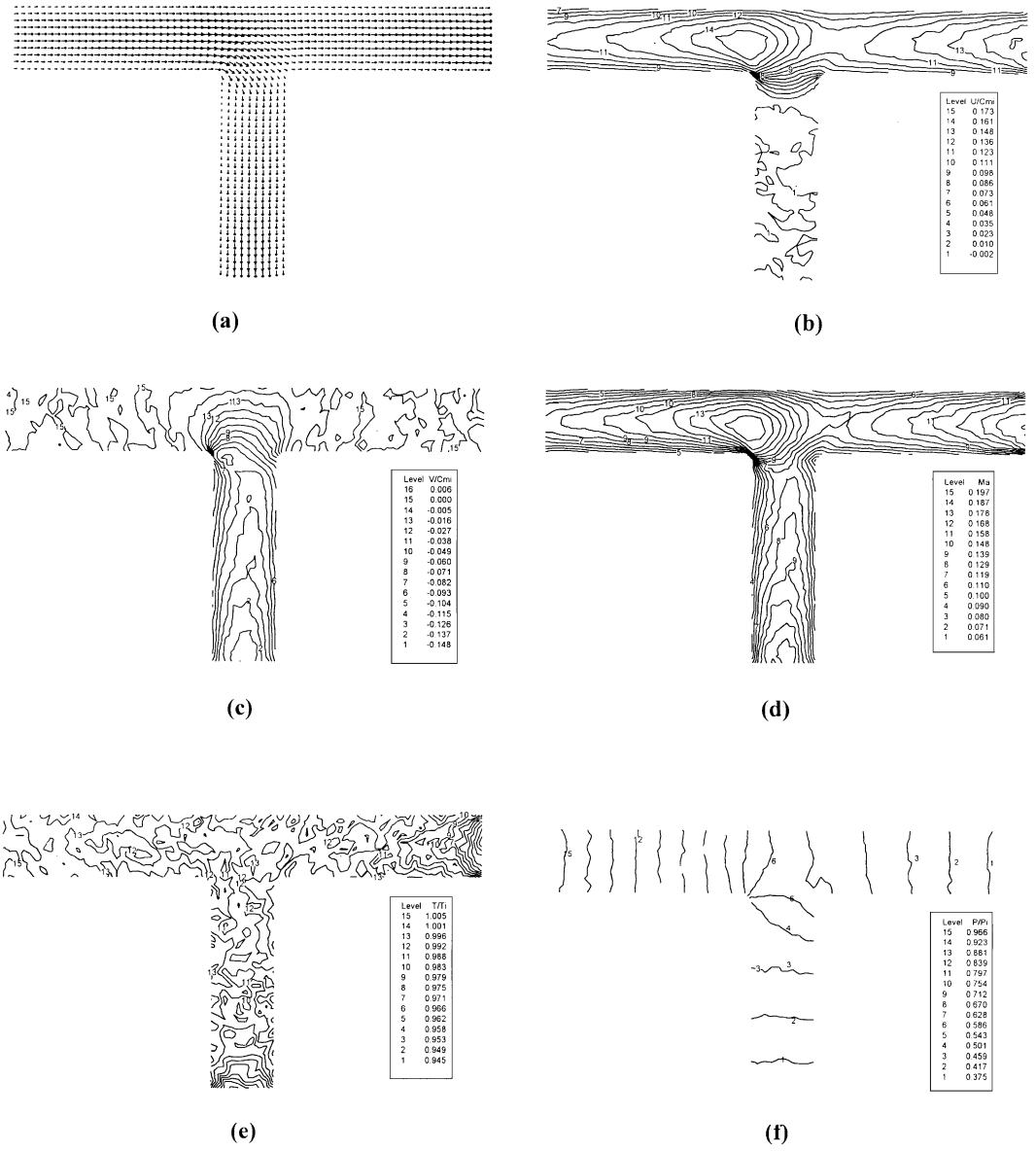

Fig. 6. The vector and contour plots of micro-manifold with P_i:P_{e1}:P_{e2} = 3:1:1 (a) vector plot (b) u-velocity (c) v-velocity (d) Mach number (e) temperature (f) pressure.

the resulting pressure ratio of exit to inlet ranges from 0.667 to 0. The "0" case refers to vacuum specified at the nozzle exit. Again, argon is used as the working gas. The resulting Knudsen number based on the inlet conditions is 0.067, while that based on exit conditions (simulated) is in the range of 0.098–0.537 (Table 3). For the vacuum case, any particles crossing the exit boundary during simulation are removed and no particles are introduced from outside this boundary, while at inlet pressure boundary particle flux conservation is imposed.

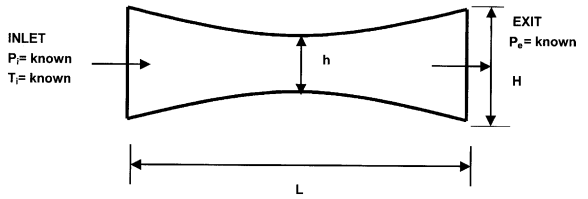

Fig. 7. Sketch of micro-nozzle (AR = 2, $L/h = 6$, $h = 1$ μm).

As shown in Table 3, the simulated centerline pressures at the cells adjacent to the nozzle inlet and exit are within 1% of those specified at the inlet and exit for $P_e/P_i \geqslant 0.143$. However, the deviation tends to deteriorate as the pressure ratio decreases. For example, for $P_e/P_i = 0.067$, the simulated gas pressure is 37.3% higher than that specified at the nozzle exit. The reasons for this over-prediction are explained as follows. The simulated pressure ratio for the vacuum case is 0.086, which is much lower (about 50%) than the value of 0.177 as predicted from isentropic supersonic expansion with an inviscid continuum analysis. For the vacuum case, supersonic speed at the exit center is also observed; however, the value is smaller than that from the continuum analysis. This result should be attributed to the viscous dissipation and two-dimensional phenomena caused by the cross-sectional area variation along the nozzle, which is neglected in the quasi-1-D inviscid continuum analysis. In addition, we can find that, for $P_e/P_i = 0.067$, the mass flow rate is nearly the same as that for vacuum case. This suggests that the predicted exit pressure should be the same as that for the vacuum case, 0.086, if the specified pressure is lower than this value. However, the predicted pressure is 0.092, which is 7% higher than 0.086. Hence, the deviation between predicted and specified pressures at the exit should be caused by the high local Knudsen number at the exit, defined as $Kn_{\Phi x} = \lambda/|\Phi/(\partial\Phi/\partial x)|$, where Φ is either temperature or u-velocity. This can be seen clearly from Table 3, which lists the local Knudsen numbers, Kn_{ux} and Kn_{Tx} at the center of the inlet and exit boundaries, respectively, at different specified pressure ratios. For example, the Kn_{ux} at the inlet (Table 3) are generally on the order of 0.01 for all pressure ratios, while those at the exit are larger due to the non-negligible u-velocity gradient and larger mean free path. The value of Kn_{ux} at the exit increases with decreasing specified pressure ratio. Similar trends are also found for Kn_{Tx} and $Kn_{\rho x}$ where both numbers are included in Table 3. In fact, it can be shown that the deviation between the particle number fluxes, based on the Chapmann–Enskog distribution function and the Maxwell–Boltzmann distribution function, is a function of both Kn_{Tx} and Kn_{ux} [8]. If we compare these results with pressure data in Table 3, we can find that the predicted exit pressure begins to deviate more from the specified value as the local Knudsen number, both Kn_{Tx} and Kn_{ux}, exceed approximately 0.05 ($P_e/P_i \leqslant 0.067$). This discrepancy increases with local exit Knudsen number (hence, decreasing specified pressure ratio) as explained previously. This high local Knudsen number makes the equilibrium Maxwell–Boltzmann distribution function problematic for introducing particles into the flow field. This definitely requires future study by using the Chapmann–Enskog distribution function, instead of the Maxwell–Boltzmann distribution function, for higher local Knudsen number pressure boundaries. Anyway, the current results confirm that the pressure boundary treatment used herein is successful for gas flows with local Knudsen numbers (both Kn_{Tx} and Kn_{ux}) less than 0.05 at the pressure boundary. Again the mass conservation at steady state between inlet and exit is excellent,

Table 3
Comparison of simulated and specified I/O pressures for micro-nozzles with AR = 2

P_e/P_i	Inlet[a]					Exit[a]						Error		
	$P_{spc.}$[b]	$P_{sim.}$[c]	$(P_{sim.}-P_{spc.})/P_{spc.}$ (%)	Kn_{Tx}	Kn_{ux}	$P_{spc.}$	$P_{sim.}$	$(P_{sim.}-P_{spc.})/P_{spc.}$ (%)	Kn_{Tx}	Kn_{ux}	Kn[d]	$(\dot{m}_i/\dot{m}_{i,vac})$	$(\dot{m}_e/\dot{m}_{i,vac})$	$(\dot{m}_e-\dot{m}_i)/\dot{m}_i$ (%)
0.667	1.0	1.001	+0.10	0.00245	0.02232	0.667	0.666	−0.15	0.00355	0.03637	0.098	0.546	0.540	−0.67
0.500	1.0	0.999	−0.10	0.00198	0.01253	0.500	0.498	−0.40	0.00735	0.02533	0.130	0.744	0.741	−0.41
0.333	1.0	0.999	−0.10	0.00199	0.01404	0.333	0.332	−0.30	0.00625	0.03614	0.191	0.893	0.895	+0.23
0.200	1.0	1.000	+0.00	0.00098	0.01000	0.200	0.198	−1.01	0.02165	0.02454	0.296	0.967	0.968	+0.20
0.143	1.0	1.002	+0.20	0.00036	0.01479	0.143	0.144	+0.70	0.03954	0.04232	0.378	0.984	0.988	+0.37
0.067	1.0	1.000	+0.00	0.00352	0.01306	0.067	0.092	+37.31	0.14590	0.16074	0.512	1.010	1.014	+0.40
0.000	1.0	0.999	−0.10	0.00146	0.01504	–	0.086	–	0.18817	0.18160	0.537	1.000	1.003	+0.26

[a] All pressure values are normalized to inlet specified pressure value, $P_i = 80.4$ kPa; $Kn_i = 0.067$.
[b] Subscript "spc." represents the specified value.
[c] Subscript "sim." represents the simulated value.
[d] Knudsen number based on local average temperature and pressure.

which shows (Table 3) that the maximum difference is less than 0.7%, although the data for $P_e/P_i = 0.067$ might be problematic. In addition, the mass flow rate increases with reduced pressure ratio and approaches a maximum value for a pressure ratio less than 0.143, as shown in both Fig. 8 and Table 3. However, this choked pressure ratio is much lower than that, 0.81, as predicted by 1-D, inviscid continuum analysis.

Figs. 9–11 illustrate the pressure ratio effects on the Mach number, v-velocity and temperature with AR = 2 at $Kn_i = 0.067$ and $p_i = 80.4$ kPa. They will be explored in detail in the following.

Fig. 9a–f illustrate the Mach number contours in micro-nozzle in the order of decreasing exit pressure with the same inlet pressure. It is clearly that the exit Mach number increases with decreasing pressure ratio as expected. From Fig. 9a–c, the centerline Mach number increases along the nozzle, a maximum value is obtained at the downstream side of the nozzle throat and then decreases further downstream in the diverging section of the nozzle. Note that the position of maximum Mach number moves further downstream as the exit pressure decreases. The exit Mach number is still subsonic for $P_e/P_i \geqslant 0.2$. This is obviously different from the continuum analysis, assuming a quasi-1-D inviscid flow, due to the viscous effects and strong rarefaction [18]. The most significant difference in results for different pressure ratios is that the viscous layer grows to the point where it completely fills the nozzle exit plane for $P_e/P_i \geqslant 0.33$. In Fig. 9d, with $P_e/P_i = 0.20$, the centerline Mach number increases all the way from the converging section to the diverging section, and a substantial Mach number, $M_e = 0.74$, is observed at the exit center. In the case of a vacuum exit (Fig. 9f), supersonic speed with Mach number of approximately 1.25 is obtained; however, as expected, it is much lower than the Mach number of 1.73 predicted from continuum analysis. Note that the data at $P_e/P_i = 0.20$ is essentially the same as that for the vacuum case, as can be seen clearly from Fig. 9e and f. The data presented in Fig. 9a fluctuate more than the other due to the lower speed involved and the inherent statistics used in the DSMC method, as explained earlier. The situation improves as pressure ratio decreases (hence, the speed

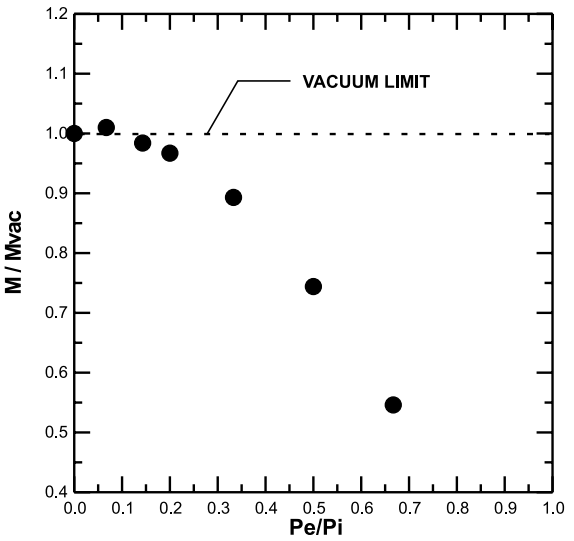

Fig. 8. Variations of normalized mass flow ratio with pressure ratio (P_e/P_i) of micro-nozzle (AR = 2).

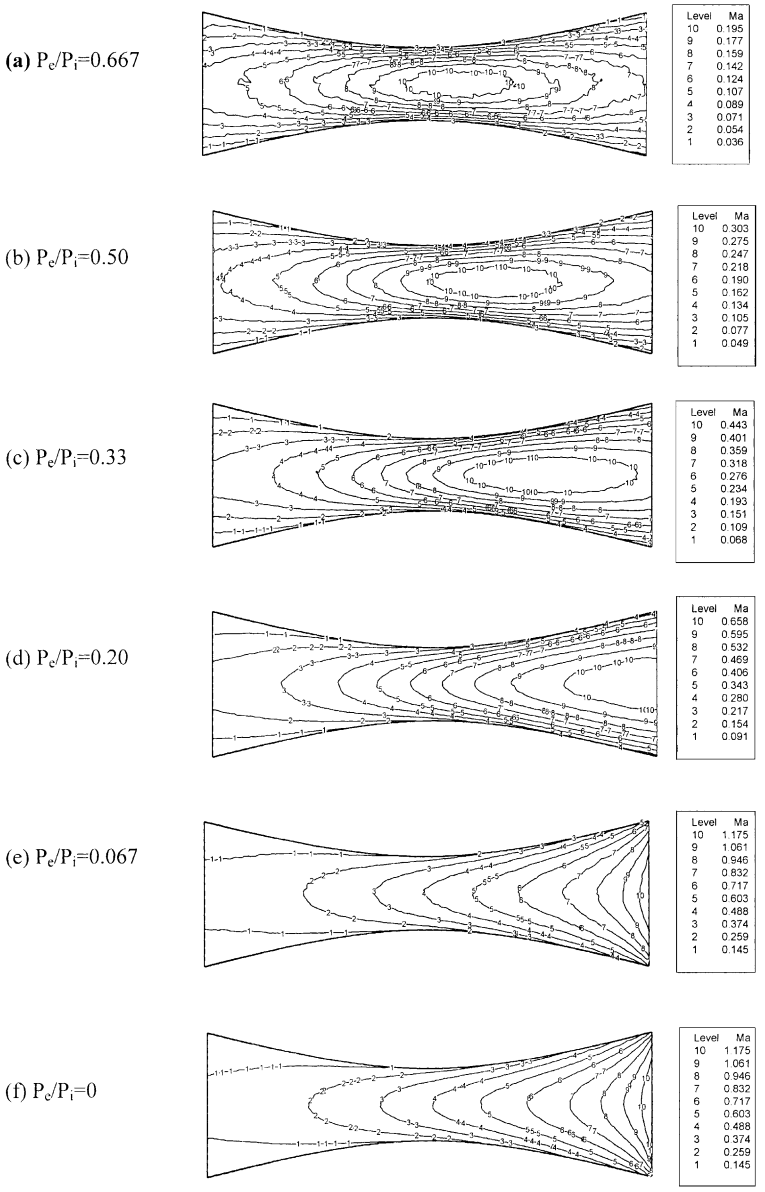

Fig. 9. Mach number contours of micro-nozzle at different pressure ratios with P_e/P_i equal to (a) 0.667 (b) 0.50 (c) 0.33 (d) 0.20 (e) 0.067 (f) 0 ($Kn_i = 0.067$, AR = 2).

increases). Appreciable slip velocities are observed along the nozzle walls. For the vacuum exit condition, Mach numbers adjacent to the wall on the order of 0.70, close to the exit, are observed (Fig. 9f). The most striking features with micro-nozzle flows is that there is no shock predicted inside the diverging part of the nozzle, as would be expected from 1-D inviscid continuum

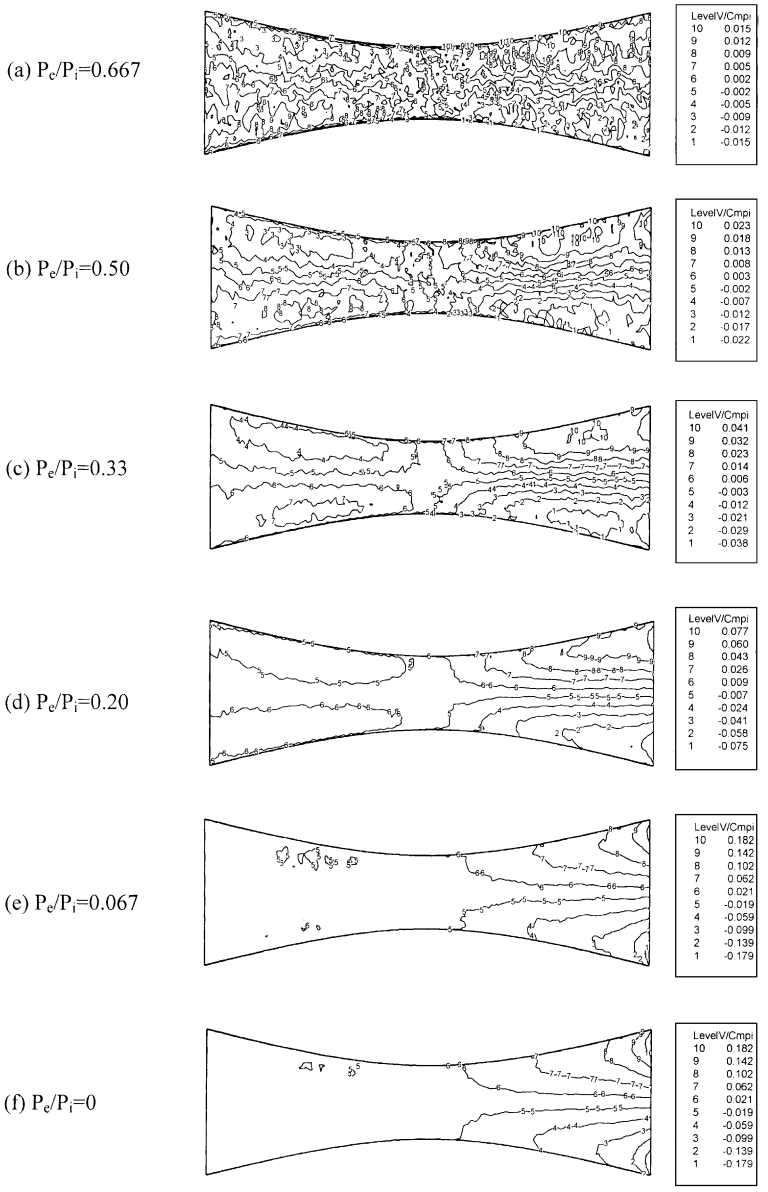

Fig. 10. v-velocity contours of micro-nozzle at different pressure ratios with P_e/P_i equal to (a) 0.667 (b) 0.50 (c) 0.33 (d) 0.20 (e) 0.067 (f) 0 ($Kn_i = 0.067, \mathrm{AR} = 2$).

analysis, for all the exit pressures considered. The absence of shocks might be due to the strong viscous and rarefaction effects, which deserves further study.

Fig. 10a–f present the v-velocity contour in the order of decreasing exit pressure. Obviously, the v-velocities are mainly caused by the geometry and flow acceleration effects. At higher pressure ratios such as those in Fig. 10a and b, the v-velocities are about one to two orders of magnitude less than the u-velocities; hence, they are essentially zero (less than 2% of inlet most probable

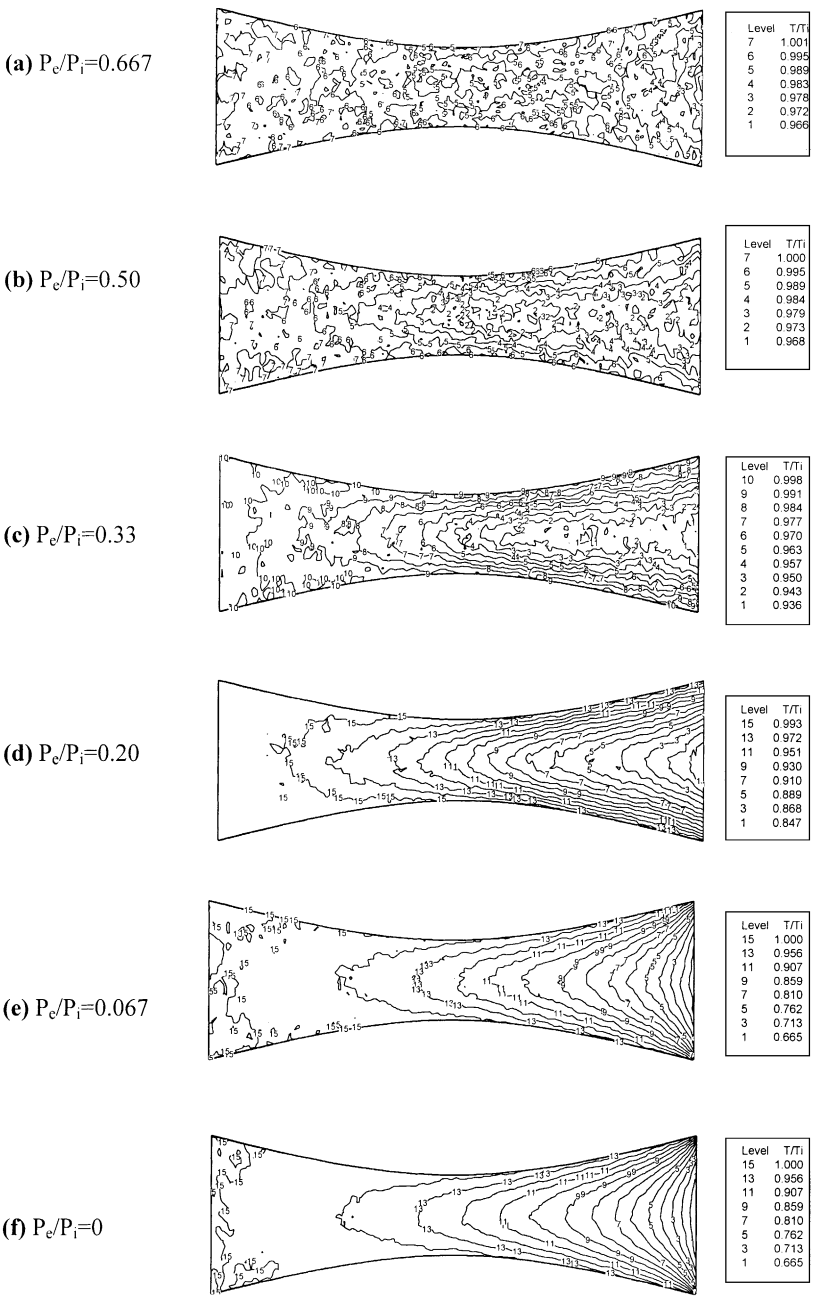

Fig. 11. Temperature contours of micro-nozzles at different pressure ratios with P_e/P_i equal to (a) 0.667 (b) 0.50 (c) 033 (d) 0.20 (e) 0.067 (f) 0 ($Kn_i = 0.067$, AR = 2).

speed) considering the statistical uncertainties in the samplings. As the pressure ratio decreases, the v-velocities remain small in the converging section and increases to some appreciable amount

in the diverging section. For example, the v-velocity at the exit can be as high as $0.18c_{mpi}$ as shown in Fig. 10f with a vacuum exit.

Temperature contours in the order of decreasing pressure ratio are shown in Fig. 11a–f. The data (Fig.11a and b) exhibit a high degree of scatter for the lower pressure ratio case, the reasons are the same as explained earlier in T-shaped micro-manifold. Temperature distribution obviously is not uniform in both spatial directions, especially in the diverging part of the nozzle. Temperature tends to decrease along the nozzle due to flow acceleration (gas expansion) as shown clearly in Fig. 11c–f. In addition, the exit temperature decreases with decreasing pressure ratio and can be as low as 0.66 times the inlet temperature, as is the case for the vacuum exit condition. Temperature jump in the converging part of the nozzle is negligible; while it becomes substantial in the diverging part of the nozzle due to the high local Knudsen number close to the walls. For example, temperature jump can grow to 0.11 times that of the inlet temperature with a vacuum exit, as shown in Fig. 11f.

3.4. Slider air bearing

The main purpose of choosing a slider air bearing as the final tested case is because of the availability of similar simulation data available in the literature and the opportunity to test pressure boundary treatment for a moving wall. In addition, this inherently high Kn number test case, also serves to identify the applicability limits of the pressure boundary treatment. The test configuration, as shown in Fig. 12, is the same as that in Alexander et al. [28] and is briefly described as follows. A hard sphere argon gas ($d_{ref} = 0.366$ nm; $\omega = 0.5$) with $T_i = 273$ K; fixed height ratio, $h_i/h_e = 2(L/h_e = 100)$, and $Ma = 0.08$ ($Kn_i = 0.625$; $h_e = 50$ nm), 0.50 ($Kn_i = 2.084$; $h_e = 15$ nm) and 1.0 ($Kn_i = 0.625$; $h_e = 50$ nm). Note that T_i is the inlet gas temperature, h_i is the inlet height of air bearing, h_e is the exit height of air bearing, L is the length of the platter, Ma is the Mach number defined by the platter speed and inlet acoustic speed, and $Kn_i = \lambda/h_i$. Although the inlet and exit pressures are both at atmospheric level (P_0), it is highly rarefied due to the nano-scale gap between the write/read head and the rotating disk.

Present simulated centerline gas pressure profiles are presented in Fig. 13 along with those obtained by Ref. [28] for comparison, where x/L is the non-dimensional location in the platter moving direction. Note that the data illustrated as lines are present simulated centerline gas pressures, while the solid symbols are present simulated wall pressures, obtained by the summation of incident and reflective momentum of particles on the write/read head surface, and the

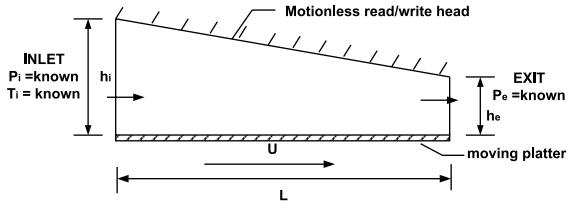

Fig. 12. Sketch of slider air bearing ($L/h_e = 100$, $h_i/h_e = 2$, $P_i = P_e = 1$ atm, where $h_e = 0.05$ μm for case I and case III, and $h_e = 0.015$ μm for case II).

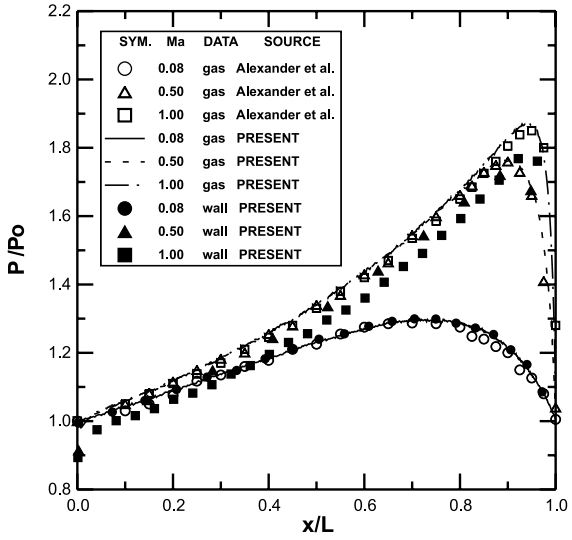

Fig. 13. Gas pressure profiles for slider air bearing at different Knudsen numbers and Mach numbers ($L = 5$ μm for case I and case III, and $L = 1.5$ μm for case II).

open symbols are gas pressures obtained in Ref. [28]. Note that gas pressure is obtained using ideal gas law, where total average temperature is used. As can be seen, the present simulated gas pressure profiles are in good agreement with those in Ref. [28] for all three cases considered. Note that only gas pressures are reported in Ref. [28]. All the predicted pressures increase at first along the air bearing, achieving the maximum values, and then decreasing rapidly at the end of the air bearing. The initial rate of increase of the gas pressures is essentially the same for $Ma \geqslant 0.5$, while the rate of decrease after the maximum pressure and the maximum value both increase with Mach number. Table 4 lists the specified, present and previous predicted gas pressures [28] and normalized mass flow rates at the inlet and exit for all cases tested. At low disk rotating speed, $Ma = 0.08$, both the predicted gas pressures at the inlet and exit coincide with specified atmospheric pressure very well. However, both the predicted gas pressures at the exit exceed those specified for high disk rotating speed cases, as $Ma \geqslant 0.5$. It seems the current prediction performs better than Ref. [28] considering the pressure difference between predicted and specified at the exit. However, it is hard to compare both, since we do not really know how they process the pressure boundaries. Similar to micro-nozzle flows, the inlet and exit local Knudsen numbers based on u-velocity and temperature gradients are also listed in Table 4. We can see that as the Kn_{ux} at the exit increases beyond 0.05 for the $Ma = 0.5$ and 1.0 cases, the gas pressure is overpredicted by about 2.3% and 9.3% at the exit, respectively. The boundary pressure deviation trend is similar to that observed for the micro-nozzle flow, although the critical value of Kn_{ux} and Kn_{Tx} is different. Comparing case II ($Kn_i = 2.08$, $Ma = 0.5$) with case III ($Kn_i = 0.63$, $Ma = 1.0$), we find that, even the Kn_{ux} of case II is higher or about the same as those of case III, the deviation of boundary pressure prediction is lower. In addition, in case I, local Knudsen numbers are on the order of 0.05, however, the deviation is negligible. This seems to suggest that this non-equilibrium caused by high local Knudsen numbers is influenced by local velocity at the pressure boundary. As

Table 4
Comparison of simulated and specified I/O pressure for thin-film air bearings

Case	Ma	Inlet[a]						Exit[a]						Error			
		$P_{spc.}$[b]	$P_{sim.}$[c]	$(P_{sim.}-P_{spc})/P_{spc.}$ (%)	Kn	Kn_{Tx}	Kn_{ux}	$P_{spc.}$	$P_{sim.}$	$(P_{sim.}-P_{spc.})/P_{spc.}$ (%)	Kn[d]	Kn_{Tx}	Kn_{ux}	$(\dot{m}_i/\dot{m}_{i,1})$	$(\dot{m}_i/\dot{m}_i)$	$(\dot{m}_e/\dot{m}_i)$	$(\dot{m}_e-\dot{m}_i)/\dot{m}_i$ (%)
I	0.08	1.0	0.999	−0.10	0.6250	0.0061	0.0410	1.0	0.999	−0.10	0.96	0.0320	0.0433	1.00	1.00	0.995	−0.50
II	0.50	1.0	0.998	−0.20	2.0835	0.0376	0.0061	1.0	1.022	+2.20	3.01	0.2780	0.8531	2.10	1.00	0.992	−0.80
III	1.00	1.0	1.003	+0.30	0.6250	0.0137	0.0177	1.0	1.093	+9.30	0.87	0.2959	0.6562	13.23	1.00	0.995	−0.50

[a] All pressure values are normalized to inlet specified pressure value, $P_i = 101.3$ kPa.
[b] Subscript "spc." represents the specified value.
[c] Subscript "sim." represents the simulated value.
[d] Subscript represents the Knudsen number based on local average temperature at the exit plane.

pointed out earlier, more research is needed to clearly identify the criterion to resolve this problem.

For a low rotating disk speed, $Ma = 0.08$, the present predicted wall pressures agree well with predicted gas pressures. This means that at low rotating disk speed, the gas particles are in thermal equilibrium, and hence the gas pressures are isotropic, resulting in the same pressure distribution both at wall and in the gas. However, at $Ma = 0.5$ and $Kn_i = 2.08$, obvious discrepancies are observed between the present predicted gas pressures and the wall pressures. The present predicted wall pressures are generally lower than the present predicted gas pressures, especially those at the inlet region. This discrepancy increases as Ma increases. The deviations between the gas pressures and the wall pressures are due to the fast moving platter speed and the highly rarefaction of the flow. Particles entering from the inlet are entrained to collide with the moving plate at the bottom such that substantial downward mean velocities (v-velocities) are formed at the inlet region. Therefore, there are comparatively fewer particles from outside the inlet colliding with the upper wall, especially near the inlet. This trend of deviation is more clear for the higher Mach number case, $Ma = 1.0$. This difference can be explained partly next by the non-equilibrium between different translational temperatures in the gas.

Fig. 14 presents the predicted ratios of translational temperature, T_x/T_y, as a function of non-dimensional location, x/L, at $Ma = 0.08$, 0.5 and 1.0. For low disk rotating speed, T_x/T_y is nearly unity, which means the flow is in thermal equilibrium. As the disk rotating speed increases up to $Ma = 0.5$, T_x/T_y attains a value of approximately 1.06, which represents a slightly non-equilibrium gas flow. A stronger non-equilibrium gas flow occurs as $Ma = 1.0$ with T_x/T_y equal to 1.15. These non-equilibrium gas flows at high rotating disk speeds explains why the wall pressures are less

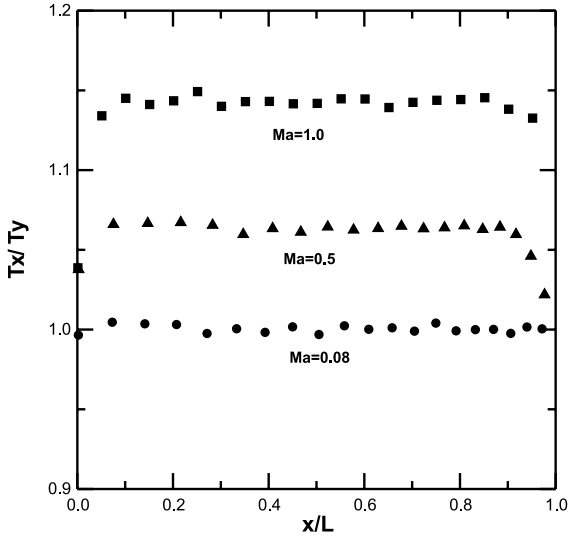

Fig. 14. Ratio of temperature components, T_x/T_y, as a function of x-position in slider air bearing for different Mach numbers ($L = 5$ μm for case I, and case III, and $L = 1.5$ μm for case II).

than the gas pressures inside the air bearing since the gas pressures are obtained by averaging the translational temperatures (hence pressures) in three directions.

4. Conclusions

This investigation has successfully developed a DSMC code using unstructured meshes. The code is verified by comparison with theoretical equilibrium collision frequency and with previous results for the temperature profiles of a 1-D normal shock. The code is then used to test the general pressure boundary treatment developed previously [23] by applying it to three different typical micro-scale (or nano-scale) gas flows, including a T-shaped micro-manifold, a micro-nozzle and a slider air bearing of computer hard drive. The major conclusions of the study are as follows.

1. The developed code is highly flexible in handling flow fields with complicated geometry without much program modification.

2. The pressure boundary treatment of Ref. [23], assuming thermal equilibrium and applying particle flux conservation, is proved successful in computing gas flows with complicated geometry, multi-exits and moving boundary at low local Knudsen numbers. However, a clear criterion for the applicability of the equilibrium Maxwell–Boltzmann distribution function requires further study.

3. Simulated results of a T-shaped micro-manifold flow show that the flow accelerates in the horizontal channel, decelerates rapidly across the corner region, and finally accelerates gradually to the horizontal exit. It is found that as the exit pressure of the vertical channel is twice that of the horizontal channel, the flow into the vertical channel is almost blocked with less than 2% of total mass flow rate.

4. Simulated results of a micro-nozzle in the transitional regime show that the flow accelerates at first and decelerates to the exit for larger pressure ratio (inlet to exit). However, the flow always accelerates along the nozzle for smaller pressure ratio. For the vacuum exit case, supersonic flow is observed; however, with smaller value compared with that of the continuum case.

5. Simulated results of a nano-scale slider air bearing show that predicted gas pressures are in good agreement with those of Ref. [28]. In general, the gas pressure increases gradually, attains a maximum value in the later portion of the air bearing and then decreases rapidly to the atmospheric level at the exit. The non-equilibrium becomes stronger as the speed (Mach number) of the moving disk increases, which makes the predicted gas pressures to deviate more from the predicted wall pressures.

6. For a micro-nozzle flow, the over-prediction of exit pressure becomes appreciable as the Kn_{ux} and Kn_{Tx} exceed approximately 0.05; however, the deviation is negligible at similar values of Kn_{ux} and Kn_{Tx} for a slider air bearing. This suggests that the applicability of the current pressure boundary treatment depends not only on the Kn_{ux} and Kn_{Tx} but also on the magnitude of interface speed at the pressure boundary.

This study raises the question of using the equilibrium Maxwell–Boltzmann distribution function in highly non-equilibrium gas flows. Also, in the current research all the particle-wall interactions are assumed to be fully diffusive, which may be suspicious for the silicone-made

micro-scale devices as shown by the experimental work of Arkilic [29]. Thus, more studies towards resolving the above two concerns are worthwhile and are currently in progress.

Acknowledgements

This investigation was supported by the National Science Council of Taiwan, Grant Nos. NSC-88-2212-E-009-019 and NSC-89-2212-E-009-034.

References

[1] Scott WB. Micromachines hold promise for aerospace. Aviation Week and Space Technology 1989;138:1–5.
[2] Trimmer WSN. Microrobots and micromechanical system. Sensors and Actuators 1989;19:267–87.
[3] Gombosi TI. Gaskinetic theory. UK: Cambridge University Press; 1994 (Chapter 5).
[4] Schaff S, Chambre P. Fundamentals of gas dynamics Princeton, NJ: Princeton University Press; 1958 (Chapter H).
[5] Mehregany M, Nagarkar P, Senturia SD, Lang JH. Operation of microfabricated harmonic and ordinary side-driven motor. IEEE Micro Electro Mechanical System Workshop, Napa Valley, CA, February 1990.
[6] Tai YC, Fan LS, Muller RS. IC-processed micro-motors: design, technology, and testing. IEEE Micro Electro Mechanical System Workshop, Salt Lake, February 1989.
[7] Tagawa N. State of the art for flying head slider mechanisms in magnetic recording disk storage. Wear 1993;168:43–7.
[8] Bird GA. Molecular gas dynamics and the direct simulation of gas flows, New York: Oxford University Press; 1994.
[9] Bird GA. Molecular gas dynamics, Oxford, England: Clarendon Press; 1976.
[10] Stefanov S, Cercignani C. Monte Carlo simulation of the Taylor-Couette flow of a rarefied gas. J Fluid Mech 1993;256:199–213.
[11] Golshtein E, Elperin T. Convective instabilities in rarefied by direct simulation Monte Carlo method. J Thermophys Heat Transf 1996;10:250–6.
[12] Nanbu K, Kubota H, Igarashi S, Urano C, Enosawa H. Application of DSMC to the design of spiral grooves on a rotor of turbomolecular pumps. Trans Jpn Soc Mech Engrs 1991;B57:172–8.
[13] Lee YK, Lee JW. Direct simulation of compression characteristics for a simple drag pump model. Vacuum 1996;47:807–9.
[14] Lee YK, Lee JW. Direct simulation of pumping characteristics for a model diffusion pump. Vacuum 1996;47:297–306.
[15] Beskok A. A model for rarefied internal gas flows. Microscale Thermophys Engng 2000, in press.
[16] Boyd ID, Jafry Y, Beukel JW. Particle simulation of helium microthruster flows. J Spacecraft Rockets 1994;31:271–81.
[17] Boyd ID, Penko PF, Meissner DL, DeWitt KJ. Experimental and numerical investigations of low-density nozzle plume flows of nitrogen. AIAA J 1992;30:2453–61.
[18] Kannenberg KC. Computational method for the direct simulation Monte Carlo technique with application to plume impingement. PhD Thesis, Cornell University, Ithaca, NY, 1998.
[19] Wilmoth RG, Lebeau GJ, Carlson AB. DSMC grid methodologies for computing low-density. Hypersonic Flow About Reusable Launch Vehicles, AIAA paper no. 96-1812, 1996.
[20] Piekos ES. Breuer KS. Numerical modeling of micromechanical devices using the direct simulation Monte Carlo method. Trans ASME J Fluids Engng 1996;118:464–9.
[21] Piekos ES. Numerical modeling of micromechanical devices using direct simulation Monte Carlo method. MS Thesis. MIT, Cambridge, USA, 1996.
[22] Nance RP, Hash DB, Hassan HA. Role of boundary conditions in Monte Carlo simulation of microelectromechanical systems. J Thermophys Heat Transf 1998;12:447–9 (Technical notes).

[23] Wu JS, Lee WS, Lee F, Wong SC. Pressure boundary treatment in internal gas flows at subsonic speed using the DSMC method. 22nd International Symposium on Rarefied Gas Dynamics, Sydney, Australia, July 9–14, 2000.
[24] Merkle CL. New possibilities and applications of Monte Carlo methods. In: Belotserkovsk II, editor. Rarefied gas dynamics, 13th International Symposium, 1985. p. 333–48.
[25] Shimada T, Abe T. Applicability of the direct simulation Monte Carlo method in a body-fitted coordinate system. In: Muntz et al., editors. Rarefied gas dynamics, Progress in Astronautics and Aeronautics, AIAA 1989. pp. 258–70.
[26] Olynick DP, Moss JN, Hassan HA. Grid generation and application for the direct simulation Monte Carlo method to the full shuttle geometry, AIAA, paper 90-1692.
[27] Wang L, Harvey JK. The application of adaptive unstructured grid technique to the computation of rarefied hypersonic flows using the DSMC method. In: Harvey J, Lord G, editors. Rarefied Gas Dynamics. 19th International Symposium, 1994. p. 843–9.
[28] Alexander FJ, Garcia AL, Alder BJ. Direct simulation Monte Carlo for thin-film bearings. Phys Fluids A 1994;6:3854–60.
[29] Arkilic EB. Measurement of the mass flow and tangential momentum accommodation coefficient in silicon micromachined channels. PhD Thesis. MIT, Cambridge, USA, 1997.